PCCP

PAPER

View Article Online
View Journal | View Issue

Cite this: *Phys. Chem. Chem. Phys.*, 2023, **25**, 18011

Location of Artinite ($Mg_2CO_3(OH)_2{\cdot}3H_2O$) within the $MgO–CO_2–H_2O$ system using *ab initio* thermodynamics†

Joshua S. Tse,[a] James Grant,[b] Jonathan M. Skelton,[c] Lisa J. Gillie,*[a] Runliang Zhu,[d] Giovanni L. Pesce,[e] Richard J. Ball,[f] Stephen C. Parker*[b] and Marco Molinari*[a]

Received 1st February 2023,
Accepted 15th June 2023

DOI: 10.1039/d3cp00518f

rsc.li/pccp

The $MgO–CO_2–H_2O$ system have a variety of important industrial applications including in catalysis, immobilisation of radionuclides and heavy metals, construction, and mineralisation and permanent storage of anthropogenic CO_2. Here, we develop a computational approach to generate phase stability plots for the $MgO–CO_2–H_2O$ system that do not rely on traditional experimental corrections for the solid phases. We compare the predictions made by several dispersion-corrected density-functional theory schemes, and we include the temperature-dependent Gibbs free energy through the quasi-harmonic approximation. We locate the Artinite phase ($Mg_2CO_3(OH)_2{\cdot}3H_2O$) within the $MgO–CO_2–H_2O$ phase stability plot, and we demonstrate that this widely-overlooked hydrated and carbonated phase is metastable and can be stabilised by inhibiting the formation of fully-carbonated stable phases. Similar considerations may apply more broadly to other lesser known phases. These findings provide new insight to explain conflicting results from experimental studies, and demonstrate how this phase can potentially be stabilised by optimising the synthesis conditions.

1. Introduction

Magnesium hydrates and carbonates within the $MgO–CO_2–H_2O$ system have a wide variety of applications including in catalysis,[1–4] the treatment of industrial carcinogenic heavy-metal waste,[5] the immobilisation of nuclear waste,[6] as fire retardants,[7] in construction,[8] in high-magnesian biogenic calcites,[9] and in carbon-mineralization reactions for permanent storage of anthropogenic carbon dioxide.[10–13] Magnesium is also one of the most abundant elements in the Earth's mantle,[14] and Mg-rich minerals are thought to exist in significant quantities on dwarf planets[15] and other extra-terrestrial bodies.[16]

Measuring phase stability is essential to predicting which material phase will form under a given set of conditions, and hence for understanding and controlling the structure and resultant properties. This problem has drawn intensive research[17] from both experiment and theory and across many fields of organic[18] and inorganic chemistry.[19–25] The stability of different phases is conceptually described by phase diagrams, which capture the relationships between equilibrium and metastable phases, the activities of component species, and external conditions including pressure, volume and temperature, in an elegant way that can be used to predict the nature and composition of a material.[26,27]

Whereas the major species in the $MgO–CO_2–H_2O$ phase diagram, such as Magnesia and Magnesite, are relatively well studied, minor phases have received comparatively less attention. One such example is the Artinite phase, which was first observed by Brugnatelli in 1902[28] and is a naturally-occurring metastable phase formed at low temperature. The crystal structure of Artinite has been analysed using X-ray diffraction[29] and the thermodynamic properties have been determined using calorimetry.[30] A few studies have also examined the thermodynamic stability of Artinite at low temperature,[31–33] but comparatively little is known on the stability of Artinite with respect to other phases in the $MgO–CO_2–H_2O$ system. Given that the materials in this

---

[a] *Department of Chemistry, University of Huddersfield, Queensgate, Huddersfield, HD1 3DH, UK. E-mail: M.Molinari@hud.ac.uk, L.J.Gillie@hud.ac.uk*

[b] *Department of Chemistry, University of Bath, Claverton Down, Bath, BA2 7AY, UK. E-mail: S.C.Parker@bath.ac.uk*

[c] *Department of Chemistry, University of Manchester, Oxford Road, Manchester, M13 9PL, UK*

[d] *CAS Key Laboratory of Mineralogy and Metallogeny, and Guangdong Provincial Key Laboratory of Mineral Physics and Materials, Guangzhou Institute of Geochemistry, Chinese Academy of Sciences, Guangzhou 510640, P. R. China*

[e] *Department of Mechanical and Construction Engineering, Northumbria University, Newcastle upon Tyne, NE1 8ST, UK*

[f] *Department of Architecture and Civil Engineering, University of Bath, Bath, BA2 7AY, UK*

† Electronic supplementary information (ESI) available. See DOI: **https://doi.org/10.1039/d3cp00518f**

system are found under a wide range of conditions, both natural and anthropogenic, a better understanding of where this phase sits within the $MgO–CO_2–H_2O$ phase diagram is potentially important to a range of disciplines.

For prediction and generation of phase diagrams, the ''brute force'' option is to use so-called global exploration methods to sample the potential-energy landscape, but this approach quickly becomes intractable as the number of variables (*i.e.* phases) increases.[34–37] When data on experimentally-identified materials and their structures is available, there are alternative, cheaper methodologies using computer simulation that can be employed whose capabilities are often overlooked.[21,38–42] The most accurate and reliable way of calculating phase diagrams, *i.e.* the current ''gold standard'' is to employ a consistent and accurate *ab initio* methodology to all the phases, so that the resulting predictions are independent of experimental thermodynamic data. It is however critical that the choice of methodology is appropriate to the system being studied (*i.e.* transferable across different material phases, which may display significant differences in chemical bonding), but also feasible given the available computational power. Transferability can be a particular challenge for systems such as $MgO–CO_2–H_2O$ that display multiple types of bonding across the phase space. For example, the bonding between Mg and different ligands (*e.g.* hydroxyl groups, water molecules and carbonate anions) is strongly ionic, whereas the intramolecular bonding within the ligands is predominantly covalent, and some of the layered magnesium hydroxides may also display interlayer van der Waals dispersion interactions.

In this work, we compare a series of different approaches, all without the inclusion of experimentally derived corrections, to construct first-principles phase stability plots for the $MgO–CO_2–H_2O$ system in order to study the thermodynamics of the under-explored Artinite phase. To account for the hierarchy of chemical bonding, we compare predictions made using density–functional theory with the popular PBE generalised-gradient approximation functional and three van der Waals corrected functionals used successfully in the literature for simulations of these materials.[43–46] We also assess the impact of using the quasi-harmonic approximation to derive the temperature dependence of the Gibbs free energy. This comprehensive study allows us to compare the predictions made from *ab initio* thermodynamic models with different approximations, and to assess the accuracy and reliability of the different flavours of DFT for studying the hydrated and carbonated phases of magnesian and other mineral systems.

2. Methodology

The VASP code[47–49] was used to carry out DFT calculations on the seven structures shown in Fig. 1. These structures are known, experimentally reported phases within the $MgO–CO_2–H_2O$ system, and are discussed in detail in the ESI.† The valence wavefunctions were described by a plane-wave basis and the core electrons were described using projected augmented-wave pseudopotentials.[50] As our baseline, we used the Perdew–Burke–Ernzerhof[51] generalised-gradient approximation (PBE GGA) to

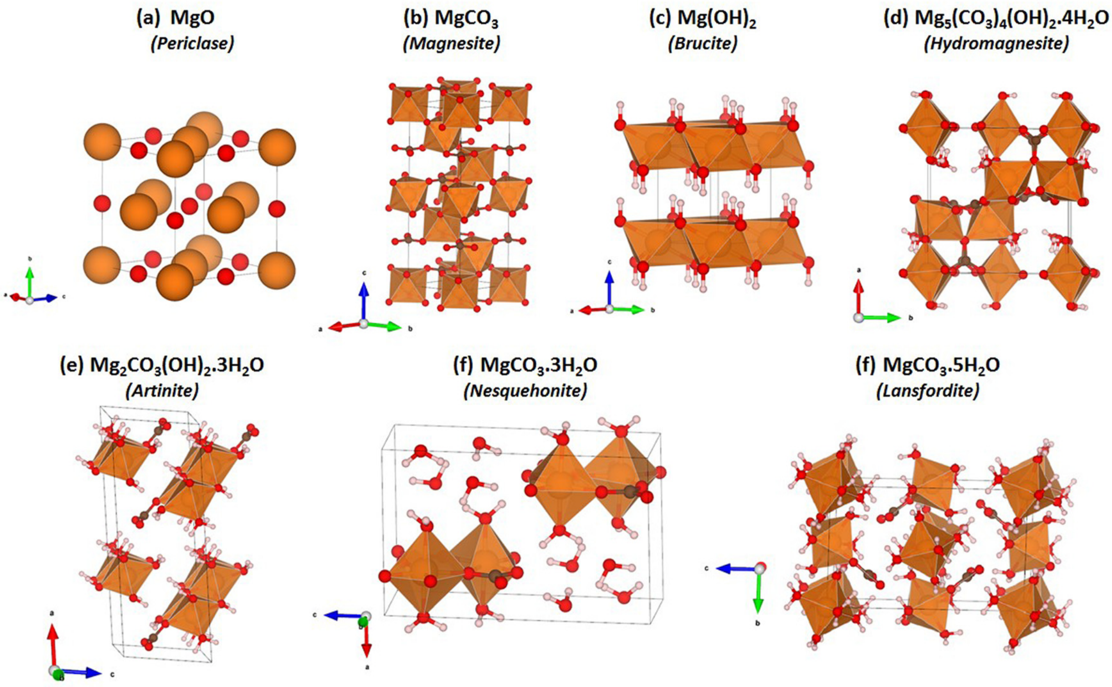

Fig. 1 Crystal structures of the Mg-rich phases in the $Mg–CO_2–H_2O$ system: (a) Periclase – MgO; (b) Magnesite – $MgCO_3$; (c) Brucite – $Mg(OH)_2$; (d) Hydromagnesite – $Mg_5(CO_3)_4(OH)_2{\cdot}4H_2O$; (e) Artinite – $Mg_2CO_3(OH)_2{\cdot}3H_2O$; (f) Nesquehonite – $MgCO_3{\cdot}3H_2O$; and (g) Lansfordite – $MgCO_3{\cdot}5H_2O$. In each structure the Mg atoms are shown in orange, C atoms in brown, H atoms in white, and O atoms in red.

model electron exchange and correlation. We also considered three different functionals including van der Waals forces, *viz.* PBE with the DFT-D3 correction (PBE-D3),[52] optB86b-vdW[53,54] and optB88-vdW.[53] These approaches are improvements over the well-established PBE-D2,[55] where a dispersion correction is computed from the atomic polarizabilities and added to the PBE total energy. In PBE-D3, the polarizability is modulated by the local environments of the atoms, and for optB86b-vdW and optB88-vdW the correction is implemented as a modification to the exchange correlation functional itself.[56] The plane-wave cut-off energy was set to 500 eV. A 4 × 4 × 4 Monkhorst-Pack *k*-point mesh was used to integrate the electronic Brillouin zone for all the phases apart from Brucite, for which a 6 × 6 × 4 *k*-point mesh was used. These settings were chosen based on explicit convergence tests on the total energies. During the electronic wavefunction optimisations the total energies were converged to 10^{-6} eV. For geometry optimisations the relaxation of the atomic structures was deemed to have converged when the forces acting on the atoms were below 10^{-2} eV Å^{-1}.

The vibrational frequencies and elastic-constant matrices were calculated using the finite-displacement routines implemented in VASP, the latter of which were used to calculate the bulk moduli by averaging the first nine elastic constants (c_{11}:c_{33}).[57–59]

For quasi-harmonic approximation (QHA) calculations, harmonic phonon calculations were performed using the Phonopy code[60] on a set of 10 expansions and contractions around the equilibrium volume (approx. ±5%). The forces were determined in a 2 × 2 × 2 supercell for all phases apart from Brucite, for which we used a 3 × 3 × 2 expansion, with VASP as the force calculator. For calculating the thermal properties, the Brillouin zone was integrated by sampling with the following regular Γ-centred *q*-point meshes, which were converged individually for each structure: 30 × 30 × 30 for Artinite, Brucite, Hydromagnesite, Lansfordite and Nesquehonite, 36 × 36 × 36 for Periclase and 48 × 48 × 48 mesh for Magnesite. Details of the QHA free energy calculations are provided in the ESI.†

The phase stability plots where generated using SurfinPy 2.[61,62] We note here several limitations in the procedure used here, *viz.*: (1) we do not account for the possibility of the coexistence of several phases, miscibility gaps, and the possible existence of different polymorphs (unless explicitly stated); (2) we similarly do not account for the possibility of unknown phases that may arise at high pressure; and (3) we do not account for the anharmonic effects that may play an important role at elevated temperature.

3. Results and discussion

3.1 Structure of $Mg_2CO_3(OH)_2{\cdot}3H_2O$ (Artinite)

$Mg_2CO_3(OH)_2{\cdot}3H_2O$ (Artinite)[63] crystallises in a monoclinic *C*2/*m* structure containing both hydroxyl and carbonate groups with Mg^{2+} in an octahedral coordination environment. The structure features Brucite ($Mg(OH)_2$)-like 1D rods with equatorial Mg–OH bonds and apical Mg–OH_2 and Mg–CO_3 bonds. In naturally-occurring Artinite the apical H_2O and CO_3^{2-} ligands are randomly distributed. However, it is not feasible to replicate this using the small unit cell used in our DFT calculations, and we have therefore constructed two models with different, fixed distributions (Fig. 2). We suggest that the most facile means to properly account for the random distribution of these groups would be classical Monte Carlo and energy-minimization techniques based on force fields, but this is beyond the scope of the present study. Both models have rows of alternating CO_3^{2-} and H_2O along the ⟨010⟩ (*b*) direction. Structure A has alternating CO_3^{2-} and H_2O along the ⟨101⟩ direction (*i.e.* on opposite octahedral faces), while structure B has either H_2O–H_2O or CO_3^{2-}–CO_3^{2-} along the ⟨101⟩ direction (*i.e.* on the same octahedral faces).

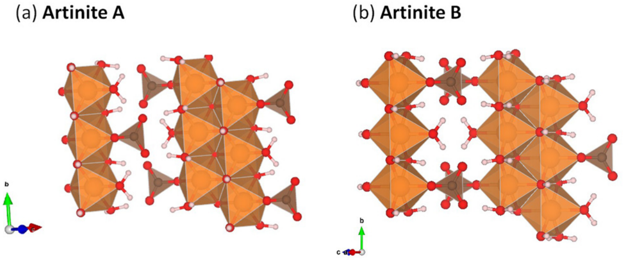
(a) Artinite A
(b) Artinite B

Fig. 2 Artinite ($Mg_2CO_3(OH)_2{\cdot}3H_2O$) structural models considered in this work, with different arrangements of the CO_3^{2-} and H_2O ligands along the ⟨101⟩ direction approximating the random distribution in the naturally-occurring material. (a) Artinite A: Alternating ligands on opposite octahedra. (b) Artinite B: Same ligands on opposite octahedra. In both structures the Mg atoms are shown in orange, C in brown, H in white and O in red.

Physical properties of the two models including the predicted lattice parameters and elastic constants are presented in Table 1. The predictions for both Artinite structures made using all four DFT techniques give generally excellent agreement with available experimental measurements, with the notable exception of a 6% underestimation of the enthalpy of formation using PBE. This highlights the importance of accurately describing vdW interactions. For both Artinite structures the DFT methods including dispersion corrections predict a decrease in the cell volume compared to experiments. We also performed similar calculations on the other phases shown in Fig. 1, and structural data and predictions of the physical properties are given in the ESI† (Tables S1–S4).

3.2 Phase stability plots of Mg-rich phases I: theoretical framework

To derive our phase stability plots, we assume that the Mg-rich phases in Fig. 1 can be formed through the reaction scheme in eqn (1):

$$x\mathrm{MgO} + y\mathrm{H_2O} + z\mathrm{CO_2} \rightarrow A \quad (1)$$

The system is in equilibrium when the chemical potentials of the reactants and products in eqn (1) are equal; *i.e.* when the change in Gibbs free energy is $\delta G_{T,p} = 0$.

$$\delta G_{T,p} = \mu_\mathrm{A} - x\mu_\mathrm{MgO} - y\mu_\mathrm{H_2O} - z\mu_\mathrm{CO_2} = 0 \quad (2)$$

Table 1 Comparison of the physical properties of Artinite measured in experiments to DFT calculations performed on the two structural models in Fig. 2: lattice constants *a*, *b*, *c* (Å), cell angles *α*, *β*, *γ* (°), volume (Å^3), enthalpy of formation ΔH_f (kJ mol^{-1}), bulk modulus *B* (GPa) and independent elastic constants (GPa)

	Expt.	optB86b-vdW		optB88-vdW		PBE-D3		PBE	
	Artinite A $Mg_2CO_3(OH)_2{\cdot}3H_2O$								
a	6.306[63]	6.28	*−0.41%*	6.284	*−0.34%*	6.303	*−0.05%*	6.371	*1.04%*
B	6.231[63]	6.113	*−1.90%*	6.116	*−1.85%*	6.109	*−1.97%*	6.186	*−0.73%*
C	16.560[63]	16.558	*−0.01%*	16.567	*0.04%*	16.598	*0.23%*	16.768	*1.25%*
$\alpha = \gamma$	90.00[63]	90	*0.00%*	90	*0.00%*	90	*0.00%*	90	*0.00%*
B	99.10[63]	97.77	*−1.39%*	97.75	*−1.41%*	97.87	*−1.29%*	98.69	*−0.46%*
Volume	642.5[63]	629.82	*−1.97%*	630.88	*−1.81%*	633.01	*−1.48%*	653.27	*1.68%*
ΔH_f	−2920.60[64]	−2896.12	*−0.01%*	−2943.26	*0.01%*	−2844.29	*−0.03%*	−2738.62	*−0.06%*
B		64.1		65.1		62.8		56.4	
*c*11		103		104		103		95	
*c*12		28		29		27		24	
*c*13		65		66		63		54	
*c*15		0		0		0		0	
*c*22		122		124		120		113	
*c*23		32		33		31		28	
*c*25		0		0		0		0	
*c*33		101		103		99		88	
*c*35		0		0		0		0	
*c*44		16		16		17		17	
*c*46		0		0		0		0	
*c*55		23		24		24		24	
*c*66		40		41		39		35	
	Artinite B ($Mg_2CO_3(OH)_2{\cdot}3H_2O$)								
a	6.306[63]	6.314	*−0.20%*	6.293	*−0.13%*	6.298	*0.12%*	6.38	*1.17%*
b	6.231[63]	6.14	*−1.34%*	6.147	*−1.28%*	6.151	*−1.46%*	6.223	*−0.14%*
c	16.560[63]	16.547	*−0.37%*	16.499	*−0.33%*	16.505	*−0.08%*	16.709	*0.90%*
$\alpha = \gamma$	90.00[63]	90	*0.00%*	90	*0.00%*	90	*0.00%*	90	*0.00%*
B	99.10[63]	98.06	*−1.22%*	97.94	*−1.23%*	97.93	*−1.10%*	98.84	*−0.31%*
Volume	642.5[63]	635.1	*−1.61%*	632.2	*−1.44%*	633.25	*−1.15%*	655.45	*2.02%*
ΔH_f	−2920.60[64]	−2843.25	*−0.01%*	−2895.72	*0.01%*	−2942.75	*−0.03%*	−2738.57	*−0.06%*
B		64.3		65.3		62.6		56.4	
*c*11		100		102		100		92	
*c*12		29		30		29		25	
*c*13		65		65		62		53	
*c*15		0		0		0		0	
*c*22		122		124		120		114	
*c*23		32		32		30		27	
*c*25		0		0		0		0	
*c*33		105		106		102		90	
*c*35		0		0		0		0	
*c*44		14		14		15		16	
*c*46		0		0		0		0	
*c*55		20		21		21		23	
*c*66		41		42		41		35	

Assuming that H_2O and CO_2 are gaseous species, μ_{CO_2} and μ_{H_2O} can be written as

$$\mu_{H_2O} = \mu^0_{H_2O} + \Delta\mu_{H_2O} \tag{3}$$

and

$$\mu_{CO_2} = \mu^0_{CO_2} + \Delta\mu_{CO_2} \tag{4}$$

The chemical potentials μ^0_x are the partial molar free energies of the reactants or products in their standard states. For an ideal gas, $\Delta\mu_x = RT\ln(p_x/p^\theta)$ where p^θ is the standard pressure of 1 bar. As both MgO and the products in eqn (1) are solid phases, we assume that:

$$\mu_{MgO} = \mu^0_{MgO} \tag{5}$$

and

$$\mu_A = \mu^0_A \tag{6}$$

Substituting eqn (3)–(6) into eqn (2), we obtain:

$$\mu^0_A - x\mu^0_{MgO} - y\mu^0_{H_2O} - z\mu^0_{CO_2} = y\Delta\mu_{H_2O} + z\Delta\mu_{CO_2} \tag{7}$$

As μ^0_A corresponds to the partial molar free energy of product A, we can replace the left-hand side of eqn (7) with the Gibbs free energy (ΔG^0_f):

$$\delta G_{T,p} = \Delta G^0_f - y\Delta\mu_{H_2O} - z\Delta\mu_{CO_2} \tag{8}$$

At equilibrium $\delta G_{T,p} = 0$, and hence:

$$\Delta G^0_f = y\Delta\mu_{H_2O} + z\Delta\mu_{CO_2} \tag{9}$$

In the case of an ideal gas:

$$\Delta G_f^0 = RT \ln((p_{H_2O})^y \cdot (p_{CO_2})^z) \quad (10)$$

We can therefore find the values of $\Delta\mu_{H_2O}$ and $\Delta\mu_{CO_2}$ (or $(p_{H_2O})^y$ and $(p_{CO_2})^z$) for which the Mg-rich phases are more or less stable than MgO. This procedure can be applied to all the solid phases to identify which is the most stable, provided that the free energy ΔG_f^0 is known for each Mg-rich phase. These free energies can be calculated using eqn (11):

$$\Delta G^0 = \sum \Delta G_f^{0,\text{products}} - \sum \Delta G_f^{0,\text{reactants}} \quad (11)$$

In this work, we calculate the free energy of each component from *ab initio* modelling, *i.e.* we do not rely on experimental thermodynamic data for any of the solid phases. This is important to provide an independent verification of experimental data and to make predictions where suitable data is not available. This approach is particularly suitable for use with structural searches, which could potentially identify previously-unreported phases. We used two approaches for calculating the formation energies of the solid phases, *viz.* the harmonic approximation (HA) and the quasi-harmonic approximation (QHA).

In the harmonic model, the free energies are calculated from:

$$G(T) = U_0 + A_{\text{phonon}}(T) = U_0 + U_{\text{ZPE}} + A_{\text{vib}}(T) \quad (12)$$

where U_0 is the calculated internal energy from a DFT calculation, U_{ZPE} is the zero point energy and $A_{\text{vib}}(T)$ is the temperature-dependent component of the vibrational Helmholtz free energy:

$$U_{\text{ZPE}} = \sum_i^{3n} \frac{R\theta_i}{2} \quad (13)$$

$$A_{\text{vib}} = \sum_i^{3n} RT \ln\left(1 - e^{-\theta_i/T}\right) \quad (14)$$

Both sums run over the $3n$ vibrational modes, where n is the number of atoms in the unit cell, with characteristic vibrational temperatures θ_i (equivalent to the frequencies in Kelvin):

$$\theta_i = \frac{h\nu_i}{k_B} \quad (15)$$

For these harmonic calculations, we make two approximations: (a) we only consider the frequencies at the Brillouin zone centre, and we therefore neglect the acoustic modes and the dispersion; and (b) we assume a fixed volume, allowing the Gibbs and Helmholtz energies to be equated.

In the QHA model, the harmonic approximation is modified to include the effect of volume changes due to thermal expansion at finite temperature. This is practically achieved by applying the harmonic approximation to a series of contracted and expanded unit cells about the equilibrium volume V_0. Using this method, the Gibbs free energy is obtained at a specific temperature T and pressure p as:[65]

$$G(T, p) = \min_v \left[U(V) + A_{\text{phonon}}(T; V) + pV\right] \quad (16)$$

where $U(V)$ is the lattice energy as a function of volume, $A_{\text{phonon}}(T;V)$ is the corresponding phonon contribution to the Helmoltz free energy, and the function is minimised with respect to volume for each value of T and p. This approximation has been shown to be appropriate up to around 2/3 of the melting temperature, beyond which anharmonic effects begin to dominate.[66,67]

For gaseous species, the standard free energy varies significantly with temperature, and as plane-wave DFT simulations are designed for condensed-phase systems we use experimental data to determine the temperature-dependent free energy term for the gaseous species:

$$G = U_0 + U_{\text{ZPE}} + (H - H^0(T) - TS_{\text{expt}}(T)) \quad (17)$$

where $H - H^0(T)$ is the experimental change in enthalpy, and $S_{\text{expt}}(T)$ is specific entropy for a given T; both terms are obtained from the NIST database.[68] Provided the free energies of the solid phases can be calculated, the phase boundaries corresponding to phase transitions can be identified using eqn (17), and we reiterate that the present method does not require any form of experimental corrections for the solid phases.[43,69]

3.3 Phase stability plots of Mg-rich phases II: free energy at T = 0 K

We first verify our methodology against an experimental phase stability plot composed of the well-characterised Mg-rich phases. Fig. 3(a) shows the phase stability plots of Brucite ($Mg(OH)_2$), Magnesite ($MgCO_3$) and Periclase (MgO) obtained from experiments, while Fig. 3(b) shows the phase stability plot containing all the Mg-rich phases predicted using optB86b-vdW. These diagrams are predicted at T = 0 K, *i.e.* the A_{vib} terms in eqn (12) are set to zero, which also simplifies eqn (17) to:

$$G = U_0 + U_{\text{ZPE}} \quad (18)$$

The phase stability plots calculated using the other functionals are included in the ESI,† Fig. S1 and S2. The $\Delta\mu_{H_2O}$ and $\Delta\mu_{CO_2}$ are varied from −2 to +1 eV, which assuming ideal-gas behaviour are equivalent to pressures of 10^{-25} bar and 10^{27} bar at 298 K. This chemical potential range is in line with previous computational work,[70] and is chosen to illustrate the difference in the free energies of the key phases.

For the experimental phase stability plot in Fig. 3(a), ΔG_f^0 is calculated using the corrected enthalpies of formation defined in eqn (19), where $\Delta H_{\text{expt}}(298\text{ K} \rightarrow 0\text{ K})$ is the change in enthalpy from 298 K to 0 K. Thermodynamic data was taken from the NIST database,[68] but experimental values are only available for these well studied phases.

$$\delta H_{\text{expt}}(0\text{ K}) = \Delta H_{\text{expt}}(298\text{ K}) - \Delta H_{\text{expt}}(298 \rightarrow 0\text{ K}) \quad (19)$$

The computed phase stability plot in Fig. 3(b) agrees relatively well with the experimental phase stability plot in Fig. 3(a), with small constant shifts in the values of p_{H_2O} and p_{CO_2}. This may indicate that a correction factor can be applied to each technique to better reproduce the experimental data.

This first test for a thermodynamic modelling strategy is to evaluate the relative stability of $Mg(OH)_2$, MgO and $MgCO_3$ following the procedure outlined in eqn (18). The triple point (where all three phases co-exist; Table 2) was calculated from

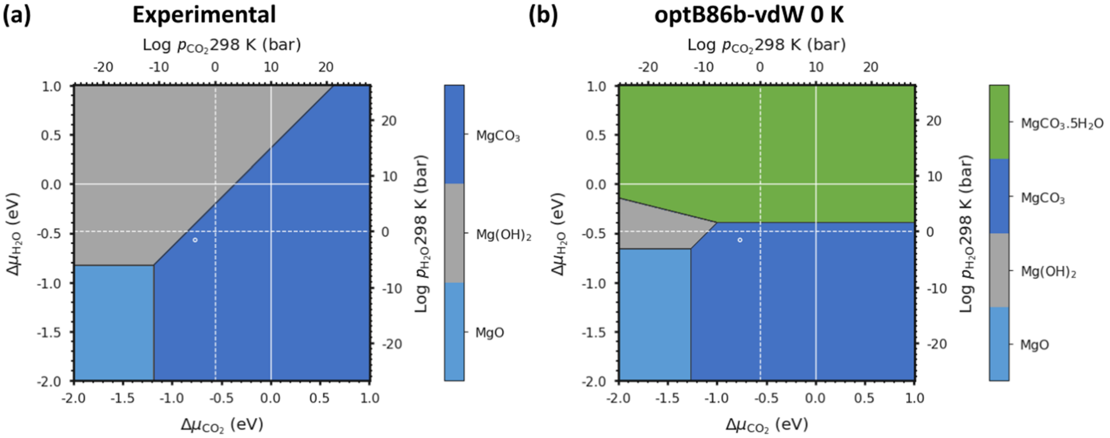

Fig. 3 (a) Phase stability plot of $Mg(OH)_2$ (Brucite), $MgCO_3$ (Magnesite) and MgO (Periclase) constructed using experimental data. (b) Predicted phase stability plot including all Mg-rich phases calculated using optB86b-vdW and eqn (18) with both solid and gaseous phases at 0 K: MgO, $MgCO_3$, $Mg(OH)_2$ and $MgCO_3{\cdot}5H_2O$. The solid and dashed white lines correspond to 1 bar pressure at 0 K and 298 K, respectively, and the white circles indicate atmospheric conditions of 400 ppm CO_2 and 32 mbar of H_2O at 298 K.

Table 2 Experimental and calculated triple points between $Mg(OH)_2$ (Brucite), $MgCO_3$ (Magnesite), MgO (Periclase) and $MgCO_3.5H_2O$ (Landsfordite), where all three phases coexist

	Temperature (K)	$\Delta\mu_{CO_2}$ (eV)	$\Delta\mu_{H_2O}$ (eV)	p_{CO_2} (bar) (298 K)	p_{H_2O} (bar) (298 K)
Brucite $Mg(OH)_2$, Magnesite $MgCO_3$ and Periclase MgO triple point					
Experimental	0	−1.18	−0.83	$10^{-10.9}$	$10^{-6.1}$
optb86B	0	−1.27	−0.66	$10^{-12.4}$	$10^{-3.1}$
Brucite $Mg(OH)_2$, Magnesite $MgCO_3$ and Lansfordite $MgCO_3{\cdot}5H_2O$ triple point					
optb86B	0	−1.00	−0.40	$10^{-9.2}$	$10^{3.0}$

the experimental data to be at $\Delta\mu_{CO_2} = -1.18$ eV and $\Delta\mu_{H_2O} = -0.83$ eV, whereas using optB86b we predict the point to occur at $\Delta\mu_{CO_2} = -1.27$ eV and $\Delta\mu_{H_2O} = -0.66$ eV. This is excellent agreement, with differences of only 0.08 eV for $\Delta\mu_{CO_2}$ and 0.17 eV for $\Delta\mu_{H_2O}$.

Due to the limited literature data on Lansfordite ($MgCO_3{\cdot}5H_2O$) and Artinite ($Mg_2CO_3(OH)_2{\cdot}3H_2O$), we are not able to include these phases on the experimental phase stability plot. However, at $p_{CO_2} = p_{H_2O} = 1$ bar at 298 K (where the dashed white lines cross in Fig. 3(b)), the most thermodynamically stable phase is predicted to be Magnesite ($MgCO_3$), whereas at $p_{CO_2} = p_{H_2O} = 1$ bar at 0 K (where the solid white lines cross in Fig. 3(b)) the predicted stable phase is Lansfordite. This agrees well with both computational[43] and experimental[71] data.

As noted above, one of our aims is to evaluate the thermodynamic stability without requiring experimental data for the condensed phases, not least as comparison with experiment is then a rigorous check on the reliability. Nevertheless, inclusion of experimentally-derived corrections does represent a valuable tool for demonstrating the viability of DFT for modelling a given system as shown in Chaka *et al.*[43] Comparing the performance of the different DFT methods, we find that optB86b-vdW gives the most accurate representation of the thermodynamics, as the triple point between the Brucite ($Mg(OH)_2$), Magnesite ($MgCO_3$) and Periclase (MgO) phases is closest to the experimental one.

3.4 Phase stability plots of Mg-rich phases III: harmonic and quasi-harmonic free energies

Accounting for the temperature dependence of the free energy in the phase stability plot, in particularly the entropy term, is important, as the most thermodynamically stable phase is likely to vary with temperature.

We choose a temperature range between 273 K and 373 K, *i.e.* where liquid water is present, which are appropriate conditions for industrial[6] and nuclear waste reprocessing[5] applications, for construction materials,[8,72] and for catalysis.[2–4] The vibrational entropy of the Mg-rich phases is included in the calculation of ΔG_f^0 for $\Delta\mu = -2$ to +1 eV, with entropies for the solid phases calculated using eqn (13)–(15) and entropies for gaseous species taken from the NIST database.[68]

We showed in the previous two sections that optB86b-vdW provides a good description of the experimental phase stability plot of the well-characterised Mg-rich phases, and that the predicted phase stability plots obtained using the different DFT methods are all shifted relative to each other. We therefore consider here only the results obtained with optB86b-vdW, but as before the phase stability plots predicted using the other DFT techniques are available in Fig. S3–S5 (ESI†) for comparison.

We organise the results in this section into three parts, showing first the free energies of Mg-rich phases at different p_{CO_2} as a function of temperature at constant $p_{H_2O} = 1$ bar, followed by the phase stability plots as a function of p_{CO_2} and

p_{H_2O} at a fixed T = 298 K, and finally the phase stability as a function of p_{CO_2} and temperature at constant p_{H_2O}.

3.5 Phase stability at constant p_{H_2O} = 1 bar

Fig. 4 compares the formation free energies of the different phases as a function of temperature, computed using optB86b-vdW with the harmonic and quasi-harmonic free energies, over the 273–373 K temperature range and a variety of p_{CO_2} with a fixed p_{H_2O} = 1 bar. These phase stability plots consider the effect of varying p_{CO_2} and thus provide insight into how this variable impacts the synthesis of the Mg-rich phases, that is, we can identify all the phases appearing at different values of p_{CO_2}, which enables us to resolve very small energy differences between phases.

At $\Delta\mu_{CO_2} = -1$ eV (low CO_2 pressure, $p_{CO_2} = 10^{-17}$ bar) and $\Delta\mu_{H_2O} = 0$ eV (p_{H_2O} = 1 bar) the most thermodynamically stable phase is predicted to be Brucite ($Mg(OH)_2$) (Fig. 4a and b). Using optB86b and the QHA free energies, Artinite shows no phase transitions at low CO_2 pressure, identified by intersections of its free-energy curve with other compounds, over the temperature range modelled. Increasing the temperature stabilises phases that contain less water per Mg^{2+} ion, due to the evaporative loss of H_2O.

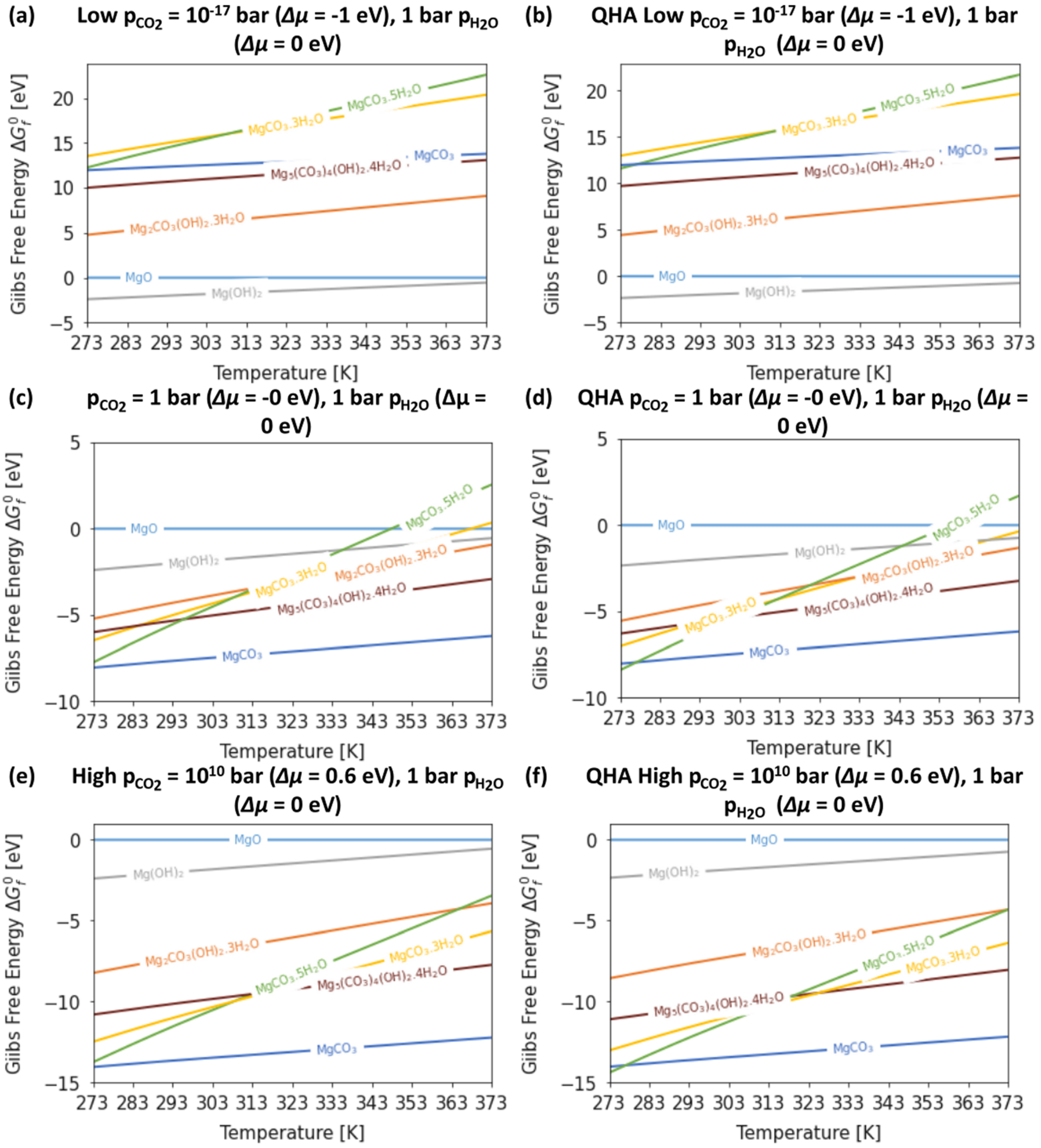
(a) Low $p_{CO_2} = 10^{-17}$ bar ($\Delta\mu$ = -1 eV), 1 bar p_{H2O} ($\Delta\mu$ = 0 eV)

(b) QHA Low $p_{CO_2} = 10^{-17}$ bar ($\Delta\mu$ = -1 eV), 1 bar p_{H2O} ($\Delta\mu$ = 0 eV)

(c) p_{CO_2} = 1 bar ($\Delta\mu$ = -0 eV), 1 bar p_{H2O} ($\Delta\mu$ = 0 eV)

(d) QHA p_{CO_2} = 1 bar ($\Delta\mu$ = -0 eV), 1 bar p_{H2O} ($\Delta\mu$ = 0 eV)

(e) High $p_{CO_2} = 10^{10}$ bar ($\Delta\mu$ = 0.6 eV), 1 bar p_{H2O} ($\Delta\mu$ = 0 eV)

(f) QHA High $p_{CO_2} = 10^{10}$ bar ($\Delta\mu$ = 0.6 eV), 1 bar p_{H2O} ($\Delta\mu$ = 0 eV)

Fig. 4 Gibbs free energy ΔG_f^0 as a function of temperature for the Mg-rich phases MgO, $MgCO_3$, $Mg(OH)_2$, $Mg_5(CO_3)_4(OH)_2\cdot4H_2O$, $Mg_2CO_3(OH)_2\cdot3H_2O$, $MgCO_3\cdot3H_2O$ and $MgCO_3\cdot5H_2O$, with $\Delta\mu_{H_2O}$ = 0 eV and (a/b) $\Delta\mu_{CO_2} = -1$ eV, (c/d) $\Delta\mu_{CO_2}$ = 0 eV, and (e/f) $\Delta\mu_{CO_2}$ = 0.6 eV, computed using the harmonic (a, c and e) and quasi-harmonic approximations (b, d and f).

The harmonic free energies predict that at $\Delta\mu_{CO_2} = \Delta\mu_{H_2O} = 0$ eV, corresponding to standard conditions with $p_{CO_2} = p_{H_2O} = 1$ bar, $MgCO_3$ is the most thermodynamically stable phase at all temperatures (Fig. 4c),[43,71] whereas the QHA predicts that Lansfordite becomes the most stable phase at 277 K (Fig. 4d). If the formation of $MgCO_3$ is kinetically inhibited, which has been demonstrated experimentally,[73] then the metastable Hydromagnesite ($Mg_5(CO_3)_4(OH)_2{\cdot}4H_2O$) phase becomes the most stable above 295 K. Under these conditions Artinite has two phase boundaries at 321 K (Artinite $Mg_2CO_3(OH)_2{\cdot}3H_2O$/Nesquehonite $MgCO_3{\cdot}3H_2O$) and 314 K (Artinite $Mg_2CO_3(OH)_2{\cdot}3H_2O$/Lansfordite $MgCO_3{\cdot}5H_2O$) (Fig. 4c). The 332 and 320 K predicted using the QHA free energies are shifted to slightly higher values (Fig. 4d).

We also compared the phase stability plots under atmospheric conditions for the different DFT techniques (Fig. S3–S5, ESI†), which all show very similar features to the phase stability plots computed under standard conditions. The predicted phase transition temperatures are tabulated in Tables S5–S7 (ESI†).

At $\Delta\mu_{CO_2} = 0.6$ eV (high CO_2 pressure, $p_{CO_2} = 10^{10}$ bar) and $\Delta\mu_{H_2O} = 0$ eV ($p_{H_2O} = 1$ bar) the most thermodynamically stable phase at all temperatures is predicted to be $MgCO_3$ (Fig. 4e), as with $p_{CO_2} = p_{H_2O} = 1$ bar (Fig. 4e and f). When the formation of $MgCO_3$ is inhibited, at $T < 290$ K Lansfordite ($MgCO_3{\cdot}5H_2O$) is predicted to be the second most stable phase, with Nesquehonite ($MgCO_3{\cdot}3\ H_2O$) favoured between 308–316 K, and $Mg_5(CO_3)_4(OH)_2{\cdot}4H_2O$ favoured only at $T > 316$ K. At high p_{CO_2} Artinite has one phase boundary at 364 K (Artinite $Mg_2CO_3(OH)_2{\cdot}3H_2O$/Lansfordite $MgCO_3{\cdot}5H_2O$). Increasing the temperature results in phase transitions associated with the loss of one H_2O per MgO unit. Again, we see a similar trend using the QHA where the phase transition temperatures are shifted ∼5–10 K higher compared to those computed using the harmonic free energies.

3.6 Phase stability of Mg-rich phases as a function of p_{CO_2} and p_{H_2O} at 298 K

Fig. 5a shows that with $p_{CO_2} = p_{H_2O} = 1$ bar the most thermodynamically stable phase is $MgCO_3$. In general, all the DFT techniques show excellent agreement, with small shifts in the predicted phase-transition pressures (see Fig. S6, ESI†). As $\Delta\mu_{CO_2}$ is increased, phases with a higher carbon content are thermodynamically stabilised, whereas increasing $\Delta\mu_{H_2O}$ stabilises the hydrated phases. As the temperature is raised from 0 to 298 K (Fig. 3), the QHA predicts that Artinite appears at the triple point between Brucite $Mg(OH)_2$, Magnesite $MgCO_3$ and Lansfordite $MgCO_3{\cdot}5H_2O$. We can also compare the predicted pressures of the triple point using the harmonic and QHA free energies. Values for the Artinite triple points obtained from the QHA are given in Table 3.

Testing the validity of these phase stability plots using experimental techniques is challenging, as changing the pressure of one reference state independently can be difficult to achieve in practice. One method is to put $MgCO_3$ under vacuum and decrease the pressure of both CO_2 and H_2O simultaneously, which would probe a diagonal line on the phase stability plot. The pressure at which $MgCO_3$ transforms to MgO could then be determined and compared to the modelling results. Alternatively, the phase stability plots could be changed to show the effect of temperature and p_{CO_2}, which we consider in the following section.

3.7 Phase stability of Mg-rich phases as a function of p_{CO_2} and temperature with a fixed $p_{H_2O} = 1$ bar

Experimental phase stability plots as a function of temperature and p_{CO_2} at 1 bar p_{H_2O} have been derived by Hill *et al.*[71] and Schott *et al.*,[74] both based on the earlier work of Langmuir *et al.*[31] Hill *et al.* results[71] predict that only Brucite ($Mg(OH)_2$) and Magnesite ($MgCO_3$) are thermodynamically stable, whereas, Schott *et al.*[74] predict that $MgCO_3$ is unstable and only forms at high temperature and high p_{CO_2}. There is only one study, by Schott *et al.*, that predicts a small region of stability for Artinite ($Mg_2CO_3(OH)_2{\cdot}3H_2O$). This contradicts Hill *et al.*,[71] although Parry *et al.*[75] have demonstrated that Artinite may be stable under conditions relevant to nuclear waste storage. It is important to note that the experimental phase stability plots predict different conditions under which phase transitions between the Mg-rich phases are expected to occur. Experimentally, $MgCO_3$ has been shown to form at 185 °C and $p_{CO_2} = 140$ bar, but the formation of

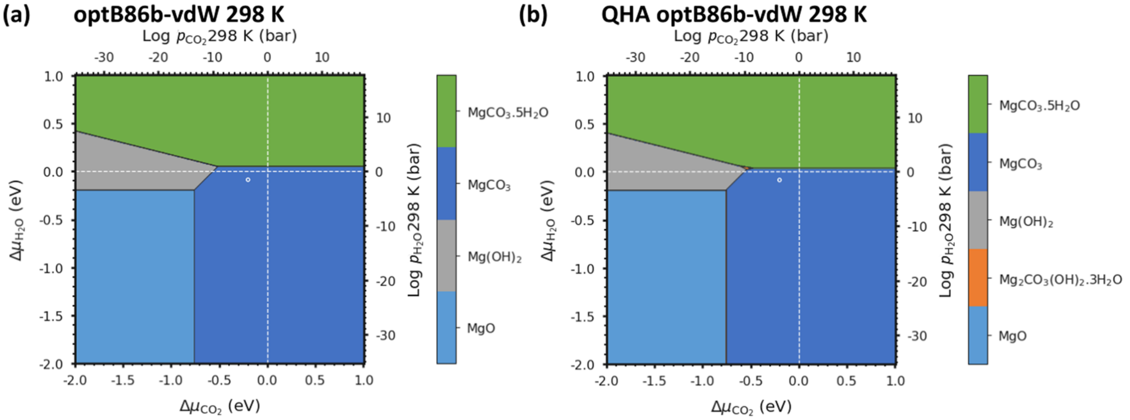

Fig. 5 Phase stability plot for the Mg-rich phases MgO, $MgCO_3$, $Mg(OH)_2$ and $MgCO_3{\cdot}5H_2O$ at 298 K computed using the harmonic (a) and quasi-harmonic free energies (b) with optB86b. The dashed white lines correspond to 1 bar p_{CO_2} and p_{H_2O} at 298 K, and the white circle represents atmospheric conditions of 400 ppm CO_2 and 32 mbar H_2O.

Table 3 Predicted triple points for the phase stability plots in Fig. 5, where three phases coexist, using optB86b and the harmonic approximation (HA) or the quasi-harmonic approximation (QHA)

	Temperature (K)	$\Delta\mu_{CO_2}$ (eV)	$\Delta\mu_{H_2O}$ (eV)	p_{CO_2} (bar) (298 K)	p_{CO_2} (bar) (298 K)
Brucite $Mg(OH)_2$, Magnesite $MgCO_3$, Periclase MgO triple point					
HA	298	−0.76	−0.20	$10^{-13.4}$	$10^{-3.4}$
QHA	298	−0.76	−0.20	$10^{-13.4}$	$10^{-3.5}$
Brucite $Mg(OH)_2$, Magnesite $MgCO_3$, Lansfordite $MgCO_3{\cdot}5H_2O$ triple point					
HA	298	−0.52	0.05	$10^{-9.1}$	$10^{0.9}$
QHA	—	—	—	—	—
Brucite $Mg(OH)_2$, Magnesite $MgCO_3$, Artinite $Mg_2CO_3(OH)_2{\cdot}3H_2O$ triple point					
HA	—	—	—	—	—
QHA	298	−0.33	0.23	$10^{-5.8}$	$10^{4.1}$
Brucite $Mg(OH)_2$, Artinite $Mg_2CO_3(OH)_2{\cdot}3H_2O$, Lansfordite $MgCO_3{\cdot}5H_2O$ triple point					
HA	—	—	—	—	—
QHA	298	−0.40	0.26	$10^{-7.0}$	$10^{4.6}$
Brucite $Mg(OH)_2$, Artinite $Mg_2CO_3(OH)_2{\cdot}3H_2O$, Magnesite $MgCO_3$ triple point					
HA	—	—	—	—	—
QHA	298	−0.29	0.24	$10^{-5.1}$	$10^{4.2}$

$MgCO_3$ at ambient temperature is virtually impossible.[76,77] As Magnesite will be the predominant phase at most CO_2 pressures in the *T vs.* p_{CO_2} phase stability plot, inhibiting its growth produces a variety of new phases. The appearance of these phases has repercussions for the sequestration of CO_2 and shows that metastable carbonate-containing phases are more important than the anhydrous magnesium carbonate (Magnesite). More generally, this has implications for applications where the evolution over time of phases in the $MgO–H_2O–CO_2$ system is an important factor, for example during the storage of industrial[6] or nuclear[5] waste materials, in construction,[8,72] where Mg binders have to remain stable over a long period of time, or during catalytic cycles where the formation of metastable phases may lead to poisoning.[2–4] Multiple phase transitions may occur during the process that ultimately leads to $MgCO_3$ formation. Indeed, Ostwald's rule[78] states that nucleation from solution occurs in steps, where the most thermodynamically unstable phases form first, followed by a step towards the most thermodynamically-stable phase. While this rule does not always hold true,[79] a larger number of phases increases the likelihood that Ostwald's rule applies.[79]

Fig. 6 compares our calculated phase stability plots as a function of temperature and $\Delta\mu_{CO_2}$ at a fixed $\Delta\mu_{H_2O}$ = 0 eV (p_{H_2O} = 1 bar), computed using the harmonic and quasi-harmonic free energies, and either including all the Mg-rich phases or with the formation of $MgCO_3$ inhibited. Comparable phase stability plots obtained using the other functionals can be found in Fig. S7 and S8 (ESI†).

Under standard p_{H_2O} and CO_2-rich conditions, using the optB86b functional and the harmonic free energies, Lansfordite ($MgCO_3{\cdot}5H_2O$) is metastable below ~310 K, above which Nesquehonite ($MgCO_3{\cdot}3H_2O$) becomes the more thermodynamically-stable phase. This prediction compares well with the work of Hill *et al.*[71] and Schott *et al.*,[74] who predict the transition to occur at 283 K. Further evidence for the existence of this transition is provided by Ming *et al.*[80] who observed that $MgCO_3{\cdot}5H_2O$ crystals dehydrate to $MgCO_3{\cdot}3H_2O$ at 285 K under atmospheric p_{H_2O} and p_{CO_2}. However, our modelling predicts these transitions to occur at higher p_{CO_2} and at temperatures of 308/312 K based on the harmonic and QHA energies. This phase transition was also investigated in a computational study by Chaka *et al.*,[43] who obtained a transition temperature of ~340 K but countered this by applying an experimental correction to the free energy of $MgCO_3{\cdot}5H_2O$. This is possibly an indication of the shortcomings of the description of van der Waals forces in DFT in general, and of the treatment in the DFT+D2 method used in that study specifically.

There is debate in the literature about the thermodynamic stability of Artinite $Mg_2CO_3(OH)_2{\cdot}3H_2O$. Our *ab initio* phase stability plots predict a small stability region for Artinite at low temperature (Fig. 6c), which is only found in some of the experimental studies.[74,75] Using the QHA free energies increases the stability of this phase over a broader range of temperatures (Fig. 6d). We note however that the complexity of the Artinite structure that arises from the random distribution of the ${CO_3}^{2-}$ and H_2O ligands is only partially considered in this study, as we use a single model structure. A random distribution would give some additional configurational entropy that would further stabilise Artinite. This is consistent with the work of Schott *et al.*,[74] which suggests that $Mg_2CO_3(OH)_2{\cdot}3H_2O$ is stable at low temperatures and low p_{CO_2}. We also note that there are multiple entropy values for $Mg_2CO_3(OH)_2{\cdot}3H_2O$ in the literature.[31,71,74] This makes it difficult to compare unambiguously our predictions to experiments, but, as our *ab initio* phase stability plots do not require any experimental corrections for the solid phases, and are therefore not biased towards particular sets of measurements, we can consider them truly predictive. With this in mind our results confirm that $Mg_2CO_3(OH)_2{\cdot}3H_2O$ is likely to remain a rare phase and one deserving of future investigation, but the favourable comparison between our predicted phase stability plots and literature data suggests that our predictions may be accurate enough to identify the synthesis conditions required to form specific Mg-rich phases.

However, we highlight a key assumption of our methodology, namely that the vibrational properties of the different phases are purely harmonic. This assumption may lead to deviation from experiment under some conditions, particularly at elevated temperature. On the other hand, using the quasi-harmonic

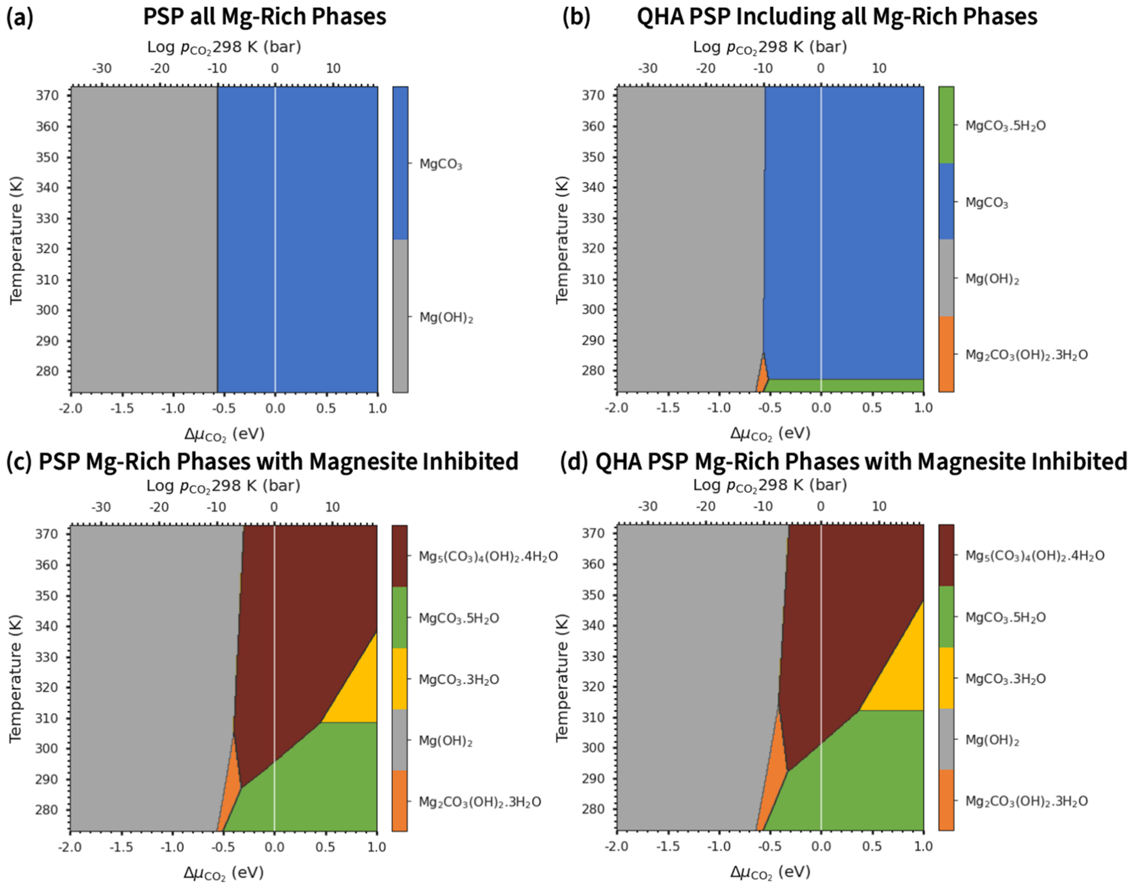

Fig. 6 Phase stability plots (PSP) as a function of $\Delta\mu_{CO_2}$ and temperature at $\Delta\mu_{H_2O}$ = 0 eV (p_{H_2O} = 1 bar), obtained using the optB86b functional and the harmonic (a and c) and quasi-harmonic free energies (QHA; b and d), and showing either all of the Mg-rich phases (a and b) or with Magnesite inhibited (c and d). On each diagram the solid white line represents p_{CO_2} = 1 bar.

approximation to account for thermal expansion, as we have done in the present study, did not significantly change the results despite a ten-fold increase in the computational cost.[81] Despite these potential shortcomings, a key advantage of this thermodynamic framework is that it can be used unambiguously to compare the DFT functionals and the different techniques to account for entropy. It could also be used with a global-exploration structure search to identify potential unknown phases and place them on the phase stability plots. Similarly, although this work examines the MgO–CO_2–H_2O system, the methodology is completely general and could be applied to a wide variety of other systems, subject to choosing an appropriate theoretical description for treating the compounds in the system under study.

4. Conclusions

In this work, we have developed an *ab initio* thermodynamics framework to situate the mineral Artinite ($Mg_2CO_3(OH)_2\cdot3H_2O$) within the phase space of other Mg hydroxides and carbonates. We find that the widely-overlooked Artinite phase is metastable and can be stabilised by inhibiting the formation of Magnesite ($MgCO_3$), thus providing an explanation for the experimental controversy over the conditions under which this rare phase can be observed.[31,71,74]

Our methodology has several advantages over alternatives, *viz.*: (1) it can identify overlooked materials that may be stable under specific conditions of temperature and partial pressures of water and carbon dioxide; (2) it can be used to identity competing and metastable phases, such as Artinite; and (3) it does not rely on the availability and accuracy of solid-phase experimental thermodynamic data. The latter in particular means that the present results can inform the future development of synthetic strategies to target and selectively stabilise specific phases of interest.

Our theoretical results also show that the inclusion of van der Waals dispersion corrections to density–functional theory is necessary to accurately predict the thermodynamic properties of the MgO–CO_2–H_2O system. Such corrections are particularly important for phases that display large numbers of hydrogen bonds, such as Artinite. On the other hand, applying the quasi-harmonic approximation does not lead to a significant improvement in the accuracy of our predictions over the harmonic approximation. Finally, we note that a potential limitation of our study is that we do not fully treat the disorder in Artinite, because of the limitations of our *ab initio* calculations, which may provide additional (entropic) stabilisation. Future work on this system should therefore consider applying classical molecular dynamics or Monte Carlo simulations to better take disorder into account.

Data availability

Raw data are available from **https://doi.org/10.17632/s96szk84zb.1**.

Author contributions

Conceptualization: JST, JMS, MM, SCP; Data curation: JST; Formal Analysis: JST, JMS; Funding acquisition: MM, LJG, SCP, RZ; Investigation: All authors; Methodology: JST, MM, SCP; Project administration: MM, SCP; Supervision: MM, LJG, SCP; Resources: MM, SCP; Validation: JST, MM, SCP; Visualization: JST, MM; Writing – original draft: JST, MM; Writing – review & editing: All authors.

Conflicts of interest

There are no conflicts to declare.

Acknowledgements

The authors would like to thank the UK Engineering and Physical Sciences Research Council (EPSRC; EP/K025597/1 and EP/R010366/1), the Royal Society (Newton Advanced Fellowship NA150190), UK Research and Innovation (UKRI; MR/T043121/1), and the Collaborative Computational Project 5 (CCP5), which is funded by the EPSRC (EP/J010480/1), for financial support. The computational work made use of the UK national HPC service, ARCHER/ARCHER2, *via* the Materials Chemistry Consortium (MCC), which is funded by the EPSRC (EP/L000202/1, EP/R029431/1 and EP/X035859/1). We also made use of the Balena HPC (University of Bath), and the Orion computing facility and the Violeta HPC (University of Huddersfield).

References

1 D. Thomele, G. R. Bourret, J. Bernardi, M. Bockstedte and O. Diwald, *Angew. Chem., Int. Ed.*, 2017, **56**, 1407–1410.
2 U. C. Rajesh, V. S. Pavan and D. S. Rawat, *ACS Sustainable Chem. Eng.*, 2015, **3**, 1536–1543.
3 G. Fan, F. Li, D. G. Evans and X. Duan, *Chem. Soc. Rev.*, 2014, **43**, 7040–7066.
4 D. Jiang, S. H. Overbury and S. Dai, *J. Phys. Chem. Lett.*, 2011, **2**, 1211–1215.
5 W. Liu, F. Huang, Y. Liao, J. Zhang, G. Ren, Z. Zhuang, J. Zhen, Z. Lin and C. Wang, *Angew. Chem., Int. Ed.*, 2008, **47**, 5619–5622.
6 S. A. Walling, H. Kinoshita, S. A. Bernal, N. C. Collier and J. L. Provis, *Dalton Trans.*, 2015, **44**, 8126–8137.
7 L. A. Hollingbery and T. R. Hull, *Polym. Degrad. Stab.*, 2010, **95**, 2213–2225.
8 P. De Silva, L. Bucea and V. Sirivivatnanon, *Cem. Concr. Res.*, 2009, **39**, 460–465.
9 J. J. M. Lenders, A. Dey, P. H. H. Bomans, J. Spielmann, M. M. R. M. Hendrix, G. de With, F. C. Meldrum, S. Harder and N. A. J. M. Sommerdijk, *J. Am. Chem. Soc.*, 2012, **134**, 1367–1373.
10 K. S. Lackner, *Science*, 2003, **300**, 1677–1678.
11 A. L. Harrison, G. M. Dipple, I. M. Power and K. U. Mayer, *Geochim. Cosmochim. Acta*, 2015, **148**, 477–495.
12 J. Matter and P. Kelemen, *Nat. Geosci.*, 2009, **2**, 837–841.
13 M. T. Dunstan, A. Jain, W. Liu, S. P. Ong, T. Liu, J. Lee, K. A. Persson, S. A. Scott, J. S. Dennis and C. P. Grey, *Energy Environ. Sci.*, 2016, **9**, 1346–1360.
14 A. Hermann and M. Mookherjee, *Proc. Natl. Acad. Sci. U. S. A.*, 2016, **113**, 13971–13976.
15 M. C. De Sanctis, E. Ammannito, A. Raponi, S. Marchi, T. B. McCord, H. Y. McSween, F. Capaccioni, M. T. Capria, F. G. Carrozzo, M. Ciarniello, A. Longobardo, F. Tosi, S. Fonte, M. Formisano, A. Frigeri, M. Giardino, G. Magni, E. Palomba, D. Turrini, F. Zambon, J. P. Combe, W. Feldman, R. Jaumann, L. A. McFadden, C. M. Pieters, T. Prettyman, M. Toplis, C. A. Raymond and C. T. Russell, *Nature*, 2015, **528**, 241–244.
16 W. M. Calvin, T. V. V. King and R. N. Clark, *J. Geophys. Res.: Planets*, 1994, **99**, 14659–14675.
17 A. Walsh, *Nat. Chem.*, 2015, **7**, 274.
18 A. Halperin, M. Kröger and F. M. Winnik, *Angew. Chem., Int. Ed.*, 2015, **54**, 15342–15367.
19 R. Gautier, X. Zhang, L. Hu, L. Yu, Y. Lin, T. O. L. Sunde, D. Chon, K. R. Poeppelmeier and A. Zunger, *Nat. Chem.*, 2015, **7**, 308–316.
20 M. Bajdich, M. García-Mota, A. Vojvodic, J. K. Nørskov and A. T. Bell, *J. Am. Chem. Soc.*, 2013, **135**, 13521–13530.
21 G. Gao, N. W. Ashcroft and R. Hoffmann, *J. Am. Chem. Soc.*, 2013, **135**, 11651–11656.
22 I. Pallikara and J. M. Skelton, *Phys. Chem. Chem. Phys.*, 2021, **23**, 19219–19236.
23 J. Zhang, H. Dong, X. Li, Z. Wang and D. Xiao, *Phys. Chem. Chem. Phys.*, 2022, **24**, 20848–20855.
24 A. J. Samin, *J. Alloys Compd.*, 2021, **879**, 160455.
25 M. Wolloch, M. E. Gruner, W. Keune, P. Mohn, J. Redinger, F. Hofer, D. Suess, R. Podloucky, J. Landers, S. Salamon, F. Scheibel, D. Spoddig, R. Witte, B. Roldan Cuenya, O. Gutfleisch, M. Y. Hu, J. Zhao, T. Toellner, E. E. Alp, M. Siewert, P. Entel, R. Pentcheva and H. Wende, *Phys. Rev. B*, 2016, **94**, 174435.
26 G. Coquerel, *Chem. Soc. Rev.*, 2014, **43**, 2286–2300.
27 P. Gallo, K. Amann-Winkel, C. A. Angell, M. A. Anisimov, F. Caupin, C. Chakravarty, E. Lascaris, T. Loerting, A. Z. Panagiotopoulos, J. Russo, J. A. Sellberg, H. E. Stanley, H. Tanaka, C. Vega, L. Xu and L. G. M. Pettersson, *Chem. Rev.*, 2016, **116**, 7463–7500.
28 S. C. L. Brugnatelli, *Rend., R. Ist. Lomb. Sci. Lett.*, 1902, **35**, 869–874.
29 H. Jagodzinski, *Tschermaks Mineral. Petrogr. Mitt.*, 1965, **10**, 297–330.
30 R. A. Hemingway and B. S. Robie, *U.S. Geol. Surv. J. Res.*, 1973, **1**, 535–546.

31 D. Langmuir, *J. Geol.*, 1965, **73**, 730–754.

32 G. Baron and J. Wyart, *Acad. Sci. Comptes rendus*, 1958, **247**, 485–487.

33 A. V. Kazakov, M. M. Tikhomirova and V. I. Plotnikova, *Int. Geol. Rev.*, 1959, **1**, 1–39.

34 S. M. Woodley and R. Catlow, *Nat. Mater.*, 2008, **7**, 937–946.

35 M. Jansen, I. V. Pentin and J. C. Schön, *Angew. Chem., Int. Ed.*, 2012, **51**, 132–135.

36 S. M. Woodley and A. A. Sokol, *Angew. Chem., Int. Ed.*, 2012, **51**, 3752–3754.

37 R. Martoák, A. Laio and M. Parrinello, *Phys. Rev. Lett.*, 2003, **90**, 75503.

38 J. Rogal, S. V. Divinski, M. W. Finnis, A. Glensk, J. Neugebauer, J. H. Perepezko, S. Schuwalow, M. H. F. Sluiter and B. Sundman, *Phys. Status Solidi B*, 2014, **251**, 97–129.

39 Y. Du, B. Wooler, M. Nines, P. Kortunov, C. S. Paur, J. Zengel, S. C. Weston and P. I. Ravikovitch, *J. Am. Chem. Soc.*, 2015, **137**, 13603–13611.

40 X. Dong, H. Zhou, H. Yang, J. Yuan, K. Jin, F. Zhou, D. Yuan, L. Wei, J. Li, X. Wang, G. Zhang and Z. Zhao, *J. Am. Chem. Soc.*, 2015, **137**, 66–69.

41 L. Malavasi, G. A. Artioli, C. Ritter, M. C. Mozzati, B. Maroni, B. Pahari and A. Caneschi, *J. Am. Chem. Soc.*, 2010, **132**, 2417–2420.

42 S. Ping Ong, L. Wang, B. Kang and G. Ceder, *Chem. Mater.*, 2008, **20**, 1798–1807.

43 A. M. Chaka and A. R. Felmy, *J. Phys. Chem. A*, 2014, **118**, 7469–7488.

44 J. Grant, G. L. Pesce, R. J. Ball, M. Molinari and S. C. Parker, *RSC Adv.*, 2016, **6**, 16066–16072.

45 D. M. S. Martins, M. Molinari, M. A. Gonçalves, J. P. Mirão and S. C. Parker, *J. Phys. Chem. C*, 2014, **118**, 27308–27317.

46 T. V. Shapley, M. Molinari, R. Zhu and S. C. Parker, *J. Phys. Chem. C*, 2013, **117**, 24975–24984.

47 G. Kresse and J. Furthmüller, *Comput. Mater. Sci.*, 1996, **6**, 15–50.

48 G. Kresse and J. Furthmüller, *Phys. Rev. B: Condens. Matter Mater. Phys.*, 1996, **54**, 11169–11186.

49 G. Kresse and J. Hafner, *Phys. Rev. B: Condens. Matter Mater. Phys.*, 1993, **47**, 558–561.

50 P. E. Blöchl, *Phys. Rev. B: Condens. Matter Mater. Phys.*, 1994, **50**, 17953–17979.

51 J. P. Perdew, K. Burke and M. Ernzerhof, *Phys. Rev. Lett.*, 1996, **77**, 3865–3868.

52 S. Grimme, J. Antony, S. Ehrlich and H. Krieg, *J. Chem. Phys.*, 2010, **132**, 154104.

53 J. Klimeš, D. R. Bowler and A. Michaelides, *Phys. Rev. B: Condens. Matter Mater. Phys.*, 2011, **83**, 195131.

54 J. Klimeš, D. R. Bowler and A. Michaelides, *J. Phys.: Condens. Matter*, 2010, **22**, 22201.

55 G. Stefan, *J. Comput. Chem.*, 2006, **27**, 1787–1799.

56 J. Klimeš and A. Michaelides, *J. Chem. Phys.*, 2012, **137**, 120901.

57 N. A. Brincat, S. C. Parker, M. Molinari, G. C. Allen and M. T. Storr, *Inorg. Chem.*, 2014, **53**, 12253–12264.

58 N. A. Brincat, S. C. Parker, M. Molinari, G. C. Allen and M. T. Storr, *Dalton Trans.*, 2015, **44**, 2613–2622.

59 M. Molinari, N. A. Brincat, G. C. Allen and S. C. Parker, *Inorg. Chem.*, 2017, **56**, 4468–4473.

60 A. Togo and I. Tanaka, *Scr. Mater.*, 2015, **108**, 1–5.

61 A. Symington, J. Tse, M. Molinari, A. Marmier and S. Parker, *J. Open Source Software*, 2019, **4**, 1210.

62 J. S. Tse, M. Molinari, S. C. Parker and A. R. Symington, *J. Open Source Software*, 2022, **7**, 4014.

63 M. Akao and S. Iwai, *Acta Crystallogr., Sect. B: Struct. Crystallogr. Cryst. Chem.*, 1977, **33**, 3951–3953.

64 R. C. Weast, *CRC Handbook of Chemistry & Physics*, CRC Press Inc., 61st edn, 1980.

65 A. Togo, L. Chaput, I. Tanaka and G. Hug, *Phys. Rev. B: Condens. Matter Mater. Phys.*, 2010, **81**, 174301.

66 L. N. Kantorovich, *Phys. Rev. B: Condens. Matter Mater. Phys.*, 1995, **51**, 3520–3534.

67 L. N. Kantorovich, *Phys. Rev. B: Condens. Matter Mater. Phys.*, 1995, **51**, 3535–3548.

68 M. W. N. I. of S. T. (U. S. Chase), NIST-JANAF Thermochemical Tables, Standard Reference Data Program National Institute of Standards and Technology, Washington, D.C. Woodbury, N.Y., 4th edn., 1998.

69 A. M. Chaka, A. R. Felmy and O. Qafoku, *Chem. Geol.*, 2016, **434**, 1–11.

70 J. P. Allen, A. Marmier and S. C. Parker, *J. Phys. Chem. C*, 2012, **116**, 13240–13251.

71 R. J. Hill, J. H. Canterford and F. J. Moyle, *Miner. Mag.*, 1982, **46**, 453–457.

72 W. S. Chiang, G. Ferraro, E. Fratini, F. Ridi, Y.-Q. Yeh, U.-S. Jeng, S.-H. Chen and P. Baglioni, *J. Mater. Chem. A*, 2014, **2**, 12991–12998.

73 M. Haenchen, V. Prigiobbe, R. Baciocchi and M. Mazzotti, *Chem. Eng. Sci.*, 2008, **63**, 1012–1028.

74 J. Schott and J. L. Dandurand, *C. R. Acad. Sci., Ser. IIc: Chim.*, 1975, **280**, 1247.

75 S. A. Parry, L. O'Brien, A. S. Fellerman, C. J. Eaves, N. B. Milestone, N. D. Bryan and F. R. Livens, *Energy Environ. Sci.*, 2011, **4**, 1457–1464.

76 F. Farhang, T. K. Oliver, M. Rayson, G. Brent, M. Stockenhuber and E. Kennedy, *Chem. Eng. J.*, 2016, **303**, 439–449.

77 K. Sandengen, L. O. Josang and B. Kaasa, *Ind. Eng. Chem. Res.*, 2008, **47**, 1002–1004.

78 W. Ostwald, *J. Phys. Chem.*, 1897, **22**, 289–330.

79 S.-Y. Chung, Y.-M. Kim, J.-G. Kim and Y.-J. Kim, *Nat. Phys.*, 2009, **5**, 68–73.

80 D. W. Ming and W. T. Franklin, *Soil Sci. Soc. Am. J.*, 1985, **49**, 1303–1308.

81 A. Erba, M. Shahrokhi, R. Moradian and R. Dovesi, *J. Chem. Phys.*, 2015, **142**, 44114.